Mon. Not. R. Astron. Soc. **387,** 998–1006 (2008) doi:10.1111/j.1365-2966.2008.13313.x

Testing the galaxy cluster mass–observable relations at $z = 1$ with *XMM–Newton* and *Chandra* observations of XLSSJ022403.9−041328⋆

B. J. Maughan,[1,2]†‡ L. R. Jones,[3] M. Pierre,[4] S. Andreon,[5] M. Birkinshaw,[2] M. N. Bremer,[2] F. Pacaud,[6] T. J. Ponman,[3] I. Valtchanov[7] and J. Willis[8]

[1]*Department of Physics, University of Bristol, Tyndall Ave, Bristol BS8 1TL*
[2]*Harvard-Smithsonian Center for Astrophysics, 60 Garden St, Cambridge, MA 02140, USA*
[3]*School of Physics and Astronomy, The University of Birmingham, Edgbaston, Birmingham B15 2TT*
[4]*Service d'Astrophysique, CEA Saclay, 91191 Gif sur Yvette, France*
[5]*INAF-Osservatorio Astronomico di Brera, Via Brera 28, 20121 Milano, Italy*
[6]*Argelander Institute for Astronomy, Bonn University, Auf dem Hügel 71, 53121 Bonn, Germany*
[7]*ESA European Space Astronomy Centre, PO Box 78, 28691 Villanueva de la Cañada, Madrid, Spain*
[8]*Department of Physics & Astronomy, University of Victoria, Elliot Building, 3800 Finnerty Road, Victoria, BC V8P 1A1, Canada*

Accepted 2008 April 9. Received 2008 April 9; in original form 2007 September 14

ABSTRACT

We present an analysis of deep *XMM–Newton* and *Chandra* observations of the $z = 1.05$ galaxy cluster XLSSJ022403.9−041328 (hereafter XLSSC 029), detected in the *XMM–Newton* Large Scale Structure survey. Density and temperature profiles of the X-ray emitting gas were used to perform a hydrostatic mass analysis of the system. This allowed us to measure the total mass and gas fraction in the cluster and define overdensity radii R_{500} and R_{2500}. The global properties of XLSSC 029 were measured within these radii and compared with those of the local population. The gas mass fraction was found to be consistent with local clusters. The mean metal abundance was $0.18^{+0.17}_{-0.15}\,Z_{\odot}$, with the cluster core regions excluded, consistent with the predicted and observed evolution. The properties of XLSSC 029 were then used to investigate the position of the cluster on the M–kT, Y_X–M and L_X–M scaling relations. In all cases the observed properties of XLSSC 029 agreed well with the simple self-similar evolution of the scaling relations. This is the first test of the evolution of these relations at $z > 1$ and supports the use of the scaling relations in cosmological studies with distant galaxy clusters.

Key words: galaxies: clusters: general – galaxies: high-redshift – intergalactic medium – cosmology: observations – X-rays: galaxies.

1 INTRODUCTION

The mass function of galaxy clusters is predicted by theoretical models of the formation of structure from the density fluctuations in the early Universe. The shape and evolution of the predicted mass function are strongly dependent on the details of the input models, and so comparison of predicted and observed mass functions at different redshifts can place tight constraints on the values of interesting cosmological parameters (e.g. Reiprich & Böhringer 2002; Vikhlinin et al. 2003; Henry 2004). However, in order to perform these tests, a key observational challenge must be met; galaxy cluster masses must be determined from their observable properties. This is an area of active research, and many approaches have been investigated using different observables, including the properties of the hot ionized intracluster medium (ICM) as measured from its X-ray emission (Sarazin 1986; Rosati, Borgani & Norman 2002) or the Sunyaev–Zel'dovich effect (Birkinshaw 1999), the distribution of properties of member galaxies such as richness and velocity dispersions and the strong and weak gravitational lensing effects of cluster gravitational potentials on background galaxies (e.g. Smith et al. 2001a; Dahle 2006). Numerical simulations of individual galaxy clusters and large cosmological volumes are also an invaluable tool for studying clusters and testing these different observational techniques (e.g. Evrard, Metzler & Navarro 1996; Nagai, Vikhlinin & Kravtsov 2007).

X-ray observations of clusters are useful because the ICM is extremely X-ray luminous, allowing the detection and study of galaxy clusters out to $z \gtrsim 1$. Under the assumption that the ICM is in hydrostatic equilibrium with the cluster's gravitational potential

⋆Based on observations obtained with *XMM–Newton*, an ESA science mission with instruments and contributions directly funded by ESA Member States and NASA.

†E-mail: ben.maughan@bristol.ac.uk
‡*Chandra* fellow.

(a reasonable assumption for clusters that are not actively merging; Poole et al. 2006) then radial profiles of the gas density and temperature measured from X-ray data can be used to determine the total cluster mass within some radius. The radius used is typically chosen to enclose an overdensity Δ with respect to the critical density at the cluster's redshift, with $\Delta = 200$ approximating to the virial radius, and $\Delta = 500$ the maximum radius detectable in typical observations. The hydrostatic mass estimation described above demands high quality X-ray data with which to measure the required profiles. Such data are becoming more commonplace in the *Chandra* and *XMM–Newton* era, but are still far from the norm. In general, and particularly for distant clusters (which provide the most information for measuring cosmological parameters), X-ray data permit the measurement of simple global properties such as a single gas temperature and luminosity. Such properties can still be useful for estimating cluster masses, as power-law scaling relations exist between global properties and cluster mass (Kaiser 1986; Markevitch 1998; Finoguenov, Reiprich & Böhringer 2001). These scaling relations are predicted by simple self-similar models of clusters. While the observed relations can differ from the self-similar predictions, the slope, normalization and evolution of the relations can be measured using high quality data, and then applied to give mass estimates for poorer quality data. These techniques have allowed studies using the temperature and luminosity functions of galaxy clusters as cosmological probes, with scaling relations used to convert between the observables and masses for comparison with theoretical mass functions.

The scaling relations are, however, an imperfect tool for converting observables to masses. Radiative cooling and cluster mergers cause significant scatter in the relations between X-ray luminosity ($L_{\rm X}$), temperature (kT) and mass, limiting the accuracy of derived masses. Much of the scatter derives from the dense core regions of clusters where radiative cooling can be extremely efficient, and the effects of mergers are most pronounced. Excluding these regions can significantly reduce the resulting scatter (Markevitch 1998; O'Hara et al. 2006; Maughan 2007). Recent work by Kravtsov, Vikhlinin & Nagai (2006) has shown that the parameter $Y_{\rm X}$, the product of gas temperature and gas mass has an extremely low scatter with total mass, providing the potential for reliable cluster mass estimates from simple observables.

The mass–observable scaling relations are reasonably well calibrated for relaxed clusters in the local Universe ($z < 0.15$; Arnaud, Pointecouteau & Pratt 2005; Vikhlinin et al. 2006), but at higher redshifts, the relations are less well measured. This is due to the long observations required to obtain sufficiently deep X-ray data to allow hydrostatic mass estimates against which to plot the simple observables. Recent work based on small samples of clusters with the best available data has enabled the measurement of the M–kT relation at $z \lesssim 0.7$ (Kotov & Vikhlinin 2005, 2006). The relations were found to have the same slope as their local counterparts, with the evolution of the normalization well described by the self-similar model. Furthermore, using some of the same data, Maughan (2007) found that the $Y_{\rm X}$–M relation at $z \sim 0.6$ is consistent with self-similar evolution of the local relation. Beyond $z \sim 0.7$, X-ray hydrostatic mass estimates have been made for only one cluster CLJ1226.9+3332, although that mass estimate may be biased by merging activity in the cluster (Maughan et al. 2007). The evolution of the mass–observable relations to such high redshifts has thus not been well studied, although more and more clusters are being detected at these distances (e.g. Rosati et al. 2004; Mullis et al. 2005; Bremer et al. 2006; Pierre et al. 2006; Stanford et al. 2006) providing a powerful resource for cosmological studies, given well-measured scaling relations. In this paper we make an important step forward in this endeavour by measuring the first X-ray hydrostatic mass for a cluster at $z > 1$ and investigating its position on the various mass–observable scaling relations.

Galaxy cluster XLSSJ022403.9−041328 (hereafter XLSSC 029) was detected as an extended X-ray source in the *XMM–Newton* Large Scale Structure (*XMM*-LSS) survey (Andreon et al. 2005; Pierre et al. 2006; Pacaud et al. 2007). The *XMM*-LSS survey is described in Pierre et al. (2004), and some results from the survey are presented in Valtchanov et al. (2004), Willis et al. (2005), Pierre et al. (2006) and Pacaud et al. (2007). Near-infrared (NIR) imaging confirmed an overdensity of faint galaxies coincident with the X-ray source XLSSC 029, and spectroscopic follow-up confirmed the redshift of the cluster to be $z = 1.05$. The cluster has since been the target of deep *Chandra* Advanced CCD Imaging Spectrometer (ACIS-S) and *XMM–Newton* follow-up observations, which are the subject of this paper. In the following sections we describe the reduction of the X-ray data, present the results of our mass analysis and investigate the location of the cluster on the different mass–observable relations. A Λ cold dark matter (ΛCDM) cosmology of $H_0 = 70\,{\rm km\,s^{-1}\,Mpc^{-1}}) \equiv 1$, and $\Omega_{\rm M} = 0.3$ ($\Omega_\Lambda = 0.7$) is adopted throughout and all errors are quoted at the 68 per cent level. In this cosmology, at $z = 1.05$, 1 arcsec corresponds to 8.1 kpc.

2 X-RAY DATA REDUCTION

The reduction and analysis methods used were the same as those presented in Maughan et al. (2007) for both the *Chandra* and *XMM–Newton* data, but the most important details are repeated here. The standard data reduction procedures were followed, using the most recent calibration products available as of 2007 March. Light curves were produced for the observations, and were cleaned to remove periods of high background. The *Chandra* observation of XLSSC 029 was taken in six consecutive exposures with cleaned exposure times of between 10 and 30 ks. The total *Chandra* exposure time was 127 ks, yielding a total of ∼1300 net source counts in the 0.3–5 keV band. The *XMM–Newton* observations had a cleaned exposure time of 70 ks (pn) and 88 ks (MOS) giving a total of ∼3400 net source counts in the 0.3–5 keV band. The observations used are summarized in Table 1.

2.1 Background preparation

For the analysis of both *Chandra* and *XMM–Newton* data, background estimates were derived from blank-sky data sets, using the same detector regions as the source emission being considered. Important differences exist between the blank-sky data and the observations of a given source due primarily to differences in the levels of the particle-induced background components (which can vary significantly with time and dominate at energies $\gtrsim$2 keV) and differences in the soft Galactic foreground emission (which can vary significantly with position on the sky and dominates at energies $\lesssim$2 keV). These differences must be corrected for when using the blank-sky data.

In the case of XLSSC 029, due to the target's high redshift, the source observations contained large detector regions that were free from source emission. Spectra were extracted from these 'local' regions and compared with the blank-sky spectra from the same detector regions.

For the *XMM–Newton* data, the blank-sky files of Carter & Read (2007) were used. Periods of high particle background were removed by filtering light curves produced in the 10–12 keV (MOS)

Table 1. Summary of the *XMM–Newton* and *Chandra* observations of XLSSC 029.

Date	Detector	Obs ID	Total exposure (ks)	Good time (ks)
2005 January 1	*XMM–Newton* pn	0210490101	86	70
2005 January 1	*XMM–Newton* MOS1	0210490101	106	87
2005 January 1	*XMM–Newton* MOS2	0210490101	106	88
2005 September 13	*Chandra* ACIS-S	6390	12	10
2005 October 12	*Chandra* ACIS-S	6394	18	18
2005 October 12	*Chandra* ACIS-S	7182	23	23
2005 October 14	*Chandra* ACIS-S	7184	23	23
2005 October 15	*Chandra* ACIS-S	7183	20	20
2005 November 21	*Chandra* ACIS-S	7185	33	33

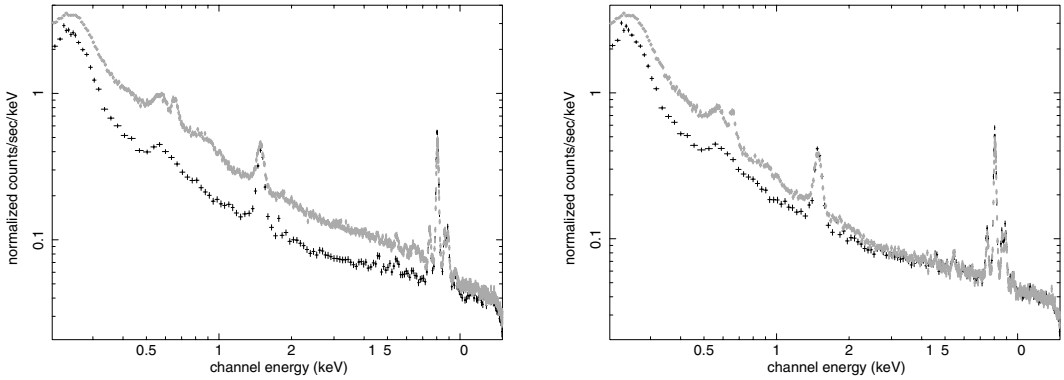

Figure 1. Comparison of the local (black points) and blank-sky (grey points) background spectra measured with the *XMM–Newton* pn camera. The two plots show the effect of filtering the blank-sky data for background flares in the high-energy band alone (left-hand plot) and of additional filtering in the 2–5 keV band (right-hand plot).

and 12–14 keV (pn) energy bands with the same count rate limits that were applied to the source data when they were cleaned. The blank-sky spectra were then normalized to match the local background count rates in these high-energy bands and compared with the local background spectra. Initially, a very poor agreement was found, and additional flare filtering at lower energies (2–5 keV, using iterative 3σ clipping of the light curve) was required for the blank-sky files before there was a good agreement between the local and blank-sky background spectra. This is illustrated for the pn camera in Fig. 1, and very similar results were found for both MOS cameras. After this additional filtering, the ratios of the entire field local to blank-sky count rates in the high-energy bands were 1.01, 1.10 and 1.14 for pn, MOS1 and MOS2, respectively, indicating that the particle background levels are similar in the target and blank-sky fields. After scaling by these factors, the *XMM–Newton* local and blank-sky spectra agreed well except below $\sim$2 keV where there was a significant decrement in all local background spectra compared to the blank-sky spectra. This is due to significantly below average soft Galactic foreground emission in the direction of XLSSC 029 and is corrected for in subsequent spectral and image analysis.

For the *Chandra* observations, the standard blank-sky background files were used.[1] The blank-sky spectra were then normalized to the local background spectra in the 9.5–12 keV band to account for variations in the particle background and compared. A good agreement was found in all of the *Chandra* observations, with no additional filtering required. Consistent with the *XMM–Newton* background spectra, there was a significant decrement at $<$2 keV in all local background spectra due to the low soft Galactic foreground emission in the direction of XLSSC 029.

[1] http://cxc.harvard.edu/contrib/maxim/acisbg/

3 IMAGE ANALYSIS

Images were produced for each data set in the 0.3–2.0 keV (observed frame) energy band, and the *Chandra* and *XMM–Newton* data were co-added to make combined images for each satellite. These images were then vignetting corrected (using an exposure map generated for 1.5−keV photons) and adaptively smoothed (Ebeling, White & Rangarajan 2006). Contours of the smoothed *Chandra* data are plotted in Fig 2, overlaid on an image produced from a 2400 s FORS2 Very Large Telescope (VLT) *I*-band exposure taken in 2005 August (proposal ID 075.A-0175, PI Andreon) with 0.7 arcsec seeing. The contour levels were defined so that the emission bounded by adjacent contours was detected at a significance of 3σ above that bounded by the surrounding contour (see Maughan et al. 2007, for details). The X-ray morphology is slightly elliptical, but appears reasonably relaxed, with no indication of substructure in the images. The X-ray morphology in the *XMM–Newton* image was consistent, with stronger contamination from point sources due to the larger point spread function (PSF). The centroid of the X-ray emission (determined from the *Chandra* data alone) is located at $\alpha[2000.0] = 02^{\rm h}24^{\rm m}4\overset{\rm s}{.}0$, $\delta[2000.0] = -04^{\circ}13'28\overset{''}{.}9$.

Wavelet decomposition was used to detect point sources in the images (Vikhlinin et al. 1998), and detected point sources were excluded from all analysis of the extended emission. There was no detection of point-like emission from the central galaxy. The X-ray

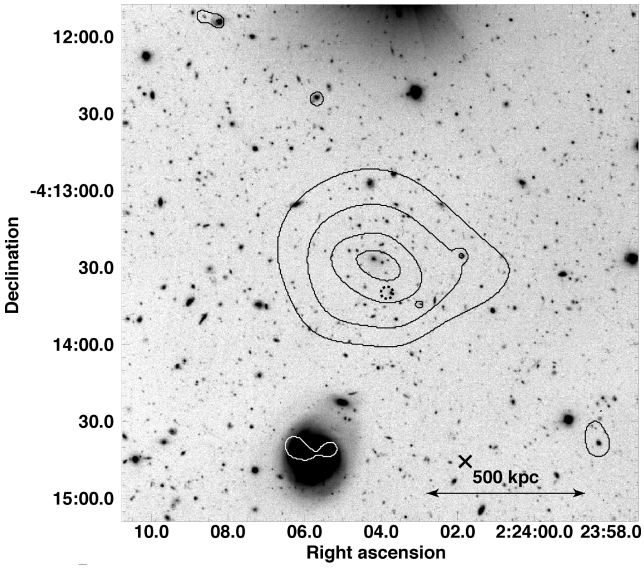

Figure 2. Contours of the adaptively smoothed image produced from the *Chandra* data are overlaid on a VLT *I*-band image of XLSSC 029. The dotted circle shows the position of the 325 MHz radio source detected by Cohen et al. (2003) with no apparent X-ray counterpart. The cross near the bottom right indicates the location of a faint X-ray point source detected in the *XMM–Newton* data that was not detected by *Chandra*.

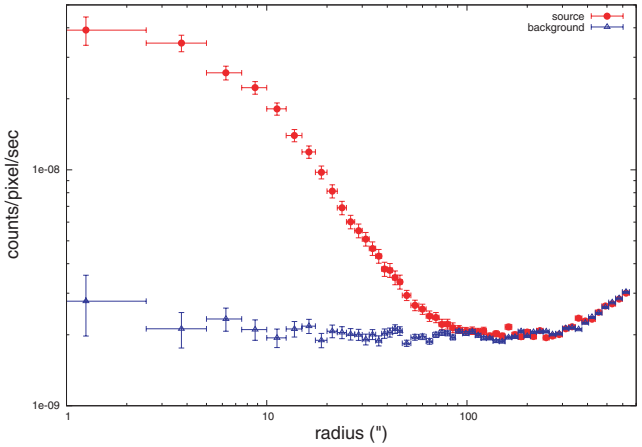

Figure 3. *XMM–Newton* surface brightness profiles of XLSSC 029 and the blank-sky background. The profiles were produced in the 0.3–2 keV band and the background profile was normalized to match the source profile in regions free of source emission.

point sources are apparent in Fig. 2 which also shows the position of a faint source detected by *XMM–Newton* but not by *Chandra*. Finally, a low-frequency radio source was detected at 325 MHz (J0224.0−0413 at $\alpha[2000.0] = 02^{\rm h}24^{\rm m}3\overset{\rm s}{.}82$, $\delta[2000.0] = -04^{\circ}13'38\overset{''}{.}8$), close to the core of XLSSC 029 by Cohen et al. (2003). No counterpart for this source was detected in either the *Chandra* or *XMM–Newton* images.

Using the *Chandra* image alone, due to the smaller PSF, the morphology of the X-ray emission was analysed quantitatively. A two-dimensional β-model was fit to the X-ray image (including instrumental effects) and the ellipticity of the best-fitting model was $e = 0.28 \pm 0.05$. The centroid shift (the standard deviation of the separation between X-ray peak and centroid) was measured to be $\langle w \rangle = (0.012 \pm 0.001)R_{500}$ (R_{500} is the radius corresponding to $\Delta = 500$ as computed in Section 4.1). These centroid shift and ellipticity values are close to the median values found for a sample of 115 galaxy clusters of a range of redshifts observed with *Chandra* (Maughan 2007). If only the more distant clusters ($z > 0.5$) from the Maughan (2007) sample are considered, then the centroid shift of XLSSC 029 is lower than 21/32 of those clusters. XLSSC 029 can thus be considered a relatively relaxed example of a distant cluster.

In order to determine the mass of gas in the cluster, a surface brightness profile was extracted from each image and converted into an emission measure profile (as described in Maughan et al. 2007). This conversion assumed a metal abundance of $0.3\,{\rm Z}_{\odot}$, and a temperature that varied with projected radius according to the mean temperature profile found by Vikhlinin et al. (2006), normalized to the global temperature and R_{500} measured for XLSSC 029 (Section 4.2). The conversion is only weakly dependent on temperature so the choice of temperature profile does not significantly affect our results.

The background level in each bin was estimated from images produced from blank-sky background files that were normalized to match the count rates in the imaging energy band in regions free of source emission. This was an iterative process, with the extent of the cluster emission being determined from the profiles and then the background images renormalized excluding this emission, with the process repeated until convergence. The background normalization is illustrated in Fig. 3, which shows the radial surface brightness profiles of the source and background (after vignetting correction) for the combined *XMM–Newton* images. Vignetting correction of the profiles was performed by dividing the counts in each bin by the sum of the exposure map counts in that bin. Note the upward curve of the profiles at large radii is due to the boosting of non-vignetted particle events by the vignetting correction. This background component is correctly subtracted, however, because the particle events are boosted in the same way for the source and background images, and level of particle events is similar in the source and background data sets (Section 2.1). The good agreement of the source and background profiles outside of the cluster emission indicate that the blank-sky background files provide an accurate background level for the emissivity profiles.

A three-dimensional (3D) model emission measure profile was then projected along the line of sight and fit simultaneously to the observed *Chandra* and *XMM–Newton* profiles. For the *XMM–Newton* data, the projected profile was convolved with a model of the *XMM–Newton* PSF before the fit statistic was computed. The PSF model used was a King function[2] with a core radius of 5.4 arcsec and a slope of 1.5. These parameters are appropriate for 1.5 keV on-axis photons and are the mean of the MOS and pn values.

The emission measure model used was the modified β-profile of Vikhlinin et al. (2006):

$$n_{\rm p}n_{\rm e} = n_0^2 \frac{(r/r_{\rm c})^{-\alpha}}{\left(1 + r^2/r_{\rm c}^2\right)^{3\beta-\alpha/2}} \left(1 + r^{\gamma}/r_{\rm s}^{\gamma}\right)^{-\epsilon/\gamma}. \quad (1)$$

The best-fitting model is plotted in Fig. 4 along with the observed profiles. The model was found to be a good fit to the combined data, with $\chi^2/\nu = 45.8/43$ demonstrating good agreement between the *Chandra* and *XMM–Newton* data. The best model parameters were $n_0 = 1.31 \times 10^{-2}\,{\rm cm}^{-3}$, $r_{\rm c} = 55.7\,{\rm kpc}$, $\alpha = 0.0$, $\beta = 0.46$, $r_{\rm s} = 872\,{\rm kpc}$ and $\epsilon = 5.0$ with γ fixed at 3. Errors were not computed on individual parameters as they are highly correlated, and model fits to Monte Carlo randomizations of the data were used to

[2] http://xmm.vilspa.esa.es/docs/documents/CAL-TN-0018.pdf

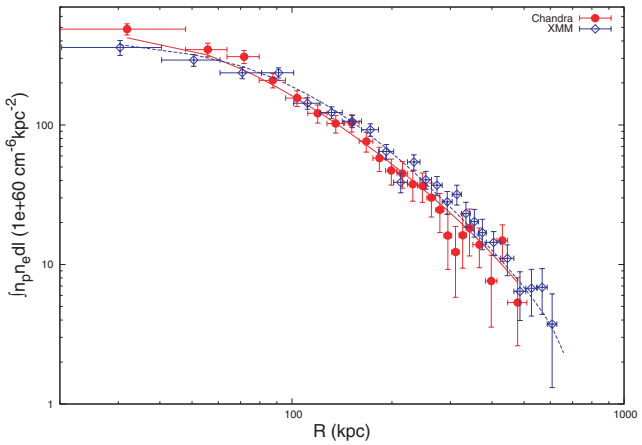

Figure 4. The emission measure profile of XLSSC 029 measured from the *Chandra* and *XMM–Newton* data are plotted along with the best-fitting model. The lines show the same 3D model projected along the line of sight, and (in the case of *XMM–Newton*) convolved with the telescope PSF.

determine the uncertainties on the gas mass and other derived properties. The gas density is related to the emission measure by $\rho_g = 1.252 m_p (n_p n_e)^{1/2}$, assuming a cosmic plasma with helium abundances given by Anders & Grevesse (1989).

While the morphology of XLSSC 029 is elliptical, our analysis assumes spherical symmetry. However, this assumption leads to negligible errors ($\lesssim$3 per cent) in the total and gas mass compared to that derived using a triaxial model (Piffaretti, Jetzer & Schindler 2003). To allow comparisons with other clusters where such detailed modelling of the gas distribution is not possible, the *Chandra* surface brightness profile was fit with a standard β-model (Cavaliere & Fusco-Femiano 1976). The best-fitting model had a core radius of $r_c = 84 \pm 5$ kpc and a slope of $\beta = 0.60 \pm 0.02$.

4 SPECTRAL ANALYSIS

The general procedure followed for the analysis of the X-ray spectra of XLSSC 029 was to extract spectra in a series of annular bins, and fit these to create a temperature profile. The temperature profile was then used to determine the mass profile of the cluster and define R_{500}. Spectra were then extracted from within this radius and fit to give the global spectral properties of the system. All spectra were modelled by an absorbed APEC model (Smith et al. 2001b), with the absorbing column fixed at the Galactic value (2.58×10^{20} cm^{-2}; Dickey & Lockman (1990). The model temperature, metal abundance and normalization were free parameters in the fits, and the source spectra were grouped to contain $\geq$30 counts per bin and fit using χ^2 minimization. For *XMM–Newton* the pn and MOS spectra were fit simultaneously with the same model, and similarly the data from the six *Chandra* observations were fit simultaneously for each region considered.

For both *Chandra* and *XMM–Newton*, background spectra were extracted from the blank-sky background files using same detector regions as the source spectra. The background spectra were normalized to match the high energy count rate in the source data sets as discussed in Section 2.1. In order to correct for the decrement in soft Galactic foreground emission towards XLSSC 029 compared to the blank-sky data, soft residual spectra were created by subtracting the blank-sky spectrum from the local background spectrum in the same, source-free detector region. In the case of *Chandra*, the residual spectra were fit with a thermal model with negative normalization. This was then included as a fixed component (scaled by extraction area) in subsequent fits to the source spectra (this method is described in more detail in Vikhlinin et al. 2005). For *XMM–Newton*, the soft residuals were scaled by extraction area and added on to the background spectra (a process known as double subtraction; see e.g. Arnaud et al. 2002). The *XMM–Newton* Science Analysis System task EVIGWEIGHT was applied to all of the *XMM–Newton* source and background events lists in order to account for differences in the telescope effective area between the source region and the region from which the soft residuals were derived. The entire analysis was also performed using a simple local background spectrum extracted from the same data set as the source spectra, and no statistically significant differences were found in any of the derived cluster properties.

4.1 Temperature and mass profiles

Spectra were extracted from annular regions centred on the cluster centroid defined so that the combined background-subtracted counts from the *XMM–Newton* pn and MOS detectors were $\geq$500 in each region. The same criterion was used to define regions for the *Chandra* data. The spectra were fit and the best-fitting temperatures are plotted in Fig. 5. The temperature profile was then fit with the following model:

$$kT(r) = kT_0 \frac{(r/r_t)^{-a}}{[1 + (r/r_t)^b]^{c/b}}. \quad (2)$$

This is the same model used by Vikhlinin et al. (2006) to fit high-quality temperature profiles of local relaxed clusters but the cool core component has been removed from the model as the data for XLSSC 029 do not require it. The model is thus a broken power law with a transition region. The model was further simplified by setting $b = c/0.45$, thereby fixing the width of the transition region to match that found in the average fit to the Vikhlinin et al. (2006) clusters. This 3D model was projected along the line of sight to predict the temperature in each bin of the observed profile. The projection weighted the different temperature components using the measured gas density profile according to the algorithm presented by Vikhlinin (2006). Because of the large radial bins used for the

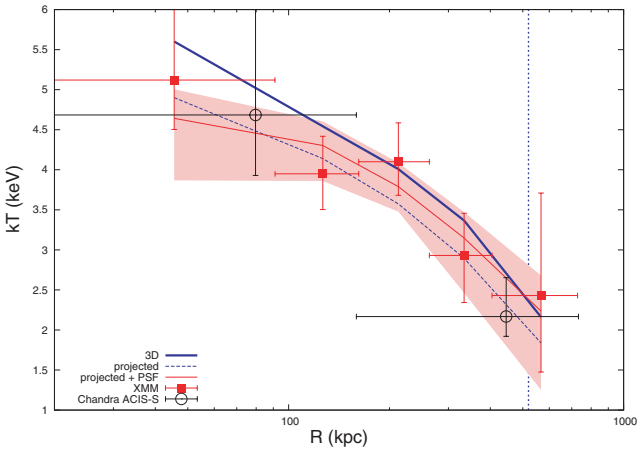

Figure 5. Projected temperature profiles measured for XLSSC 029 using *XMM–Newton* and *Chandra*. The curves show the best-fitting 3D model, its projection and the final model after PSF convolution, with the 1σ errors on the projected model shown by the shaded region. The model was fit to the *XMM–Newton* data alone, and the vertical line indicates R_{500}.

Chandra data, and to simplify the projection calculation, only the *XMM–Newton* data were used for fitting the temperature profile.

The *XMM–Newton* PSF is not negligible compared to the size of the radial bins used for the temperature profile. The effect of the PSF is to redistribute some photons that were emitted in one projected annulus into a different projected annulus. The magnitude of this effect was computed by using a background subtracted *Chandra* image of XLSSC 029 to provide the projected photon distribution with no PSF redistribution. For each annular region in the temperature profile, a subimage was extracted, containing just the photons in that region. This subimage was then convolved with an image of the *XMM–Newton* PSF (a PSF suitable for 1.5 keV photons detected on-axis was used), and the number of photons redistributed from that annulus into each other annulus was measured. This process gave a redistribution matrix describing the relative contribution of each projected annular region to each bin in the final, projected, PSF-convolved profile. In the fitting procedure, the temperature in each bin in the final model profile was calculated by a second application of the Vikhlinin (2006) algorithm to combine the contributions from every projected bin, weighted by the PSF redistribution factors.

The best-fitting 3D model, its projection and the final model including PSF convolution are plotted in Fig. 5. The best-fitting model had parameters $kT_0 = 3.5$ keV, $r_t = 586$ kpc, $a = 0.20$ and $c = 1.55$. The probability distributions of the parameters were determined by fits to Monte Carlo randomizations of the data, and used to determine uncertainties on derived cluster properties. The best-fitting 3D model was also compared with the *Chandra* data plotted in Fig. 5. The projected temperature predicted by the 3D model for the inner and outer *Chandra* temperature bins is 4.6 and 2.8 keV. The prediction for inner bin agrees well with the measured value, while that for the outer bin is slightly (but not significantly) higher than the observed value ($2.2^{+0.5}_{-0.2}$ keV).

The best-fitting 3D models for the gas density and temperature profiles were then used to compute the total mass profile of XLSSC 029 under the assumption of hydrostatic equilibrium, propagating the Monte Carlo uncertainties to all derived properties. This profile was then used to compute the overdensity profile of the system and determine $R_{500} = 0.52^{+0.10}_{-0.05}$ Mpc and $R_{2500} = 0.23^{+0.06}_{-0.02}$ Mpc. The derived mass profile of XLSSC 029 is plotted in Fig. 6, along with the gas mass profile. The total mass of the system within R_{500} was found to be $1.3^{+0.9}_{-0.3} \times 10^{14}\,\mathrm{M}_\odot$. The gas mass fraction ($f_{\rm gas}$) profile of XLSSC 029 is plotted in Fig. 7. At R_{500} the gas mass fraction was $0.14^{+0.02}_{-0.05}$, and within the smaller radius of R_{2500} the gas fraction was $0.08^{+0.01}_{-0.02}$.

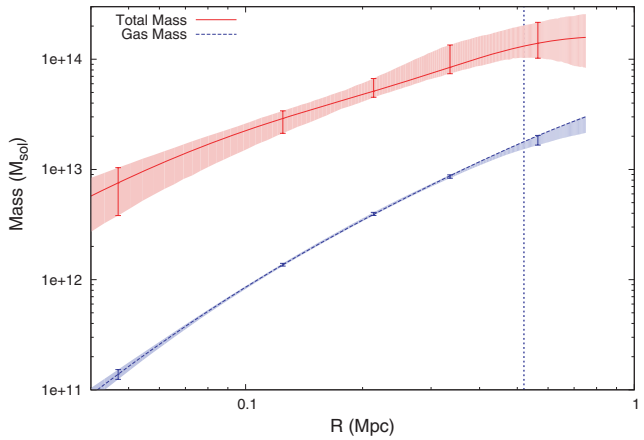

Figure 6. Profiles of the derived total and gas mass in XLSSC 029. The 1σ errors on the models are shown by the shaded region, the data points mark the mid-points of the *XMM–Newton* temperature profile bins and the vertical line indicates R_{500}.

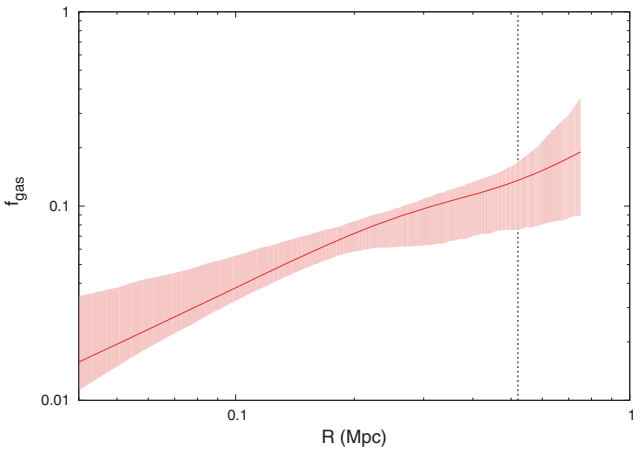

Figure 7. Profiles of the gas mass fraction in XLSSC 029. The 1σ errors are shown by the shaded region and the vertical line indicates R_{500}.

4.2 Global spectral properties

With R_{500} determined from the mass analysis, the integrated spectral properties of XLSSC 029 were then measured within that aperture. The central $0.15R_{500}$ was excluded, as the emission from this region can be affected by strong radiative cooling and merger events, leading to enhanced scatter from the self-similar cluster scaling relations (e.g. Maughan 2007). The *XMM–Newton* and *Chandra* data were fit separately. The emission-weighted temperature of the gas within R_{500} was found to be $3.4^{+0.3}_{-0.2}$ keV based on the combined *XMM–Newton* data, and $4.3^{+1.1}_{-0.7}$ keV from the combined *Chandra* observations. The metallicity (iron abundances relative to the solar values of Anders & Grevesse 1989) of the gas was measured to be $0.18^{+0.17}_{-0.15}\,\mathrm{Z}_\odot$ from the *XMM–Newton* data. While the data did not permit a metallicity profile of the cluster, the value measured with the core regions included increased slightly to $0.40^{+0.17}_{-0.16}\,\mathrm{Z}_\odot$, perhaps indicative of an abundance peak in the core. The *Chandra* data were not able to provide useful constraints on the metallicity.

The bolometric X-ray luminosity of the cluster within R_{500} was measured using the data from each satellite. The *XMM–Newton* data gave $L_{\rm X} = (3.4 \pm 0.4) \times 10^{44}\,\mathrm{erg\,s^{-1}}$ [$L_{\rm X} = (4.6 \pm 0.4) \times 10^{44}\,\mathrm{erg\,s^{-1}}$ with the central $0.15\,R_{500}$ included], while the *Chandra* data gave $L_{\rm X} = 3.0^{+1.0}_{-0.6} \times 10^{44}\,\mathrm{erg\,s^{-1}}$ ($L_{\rm X} = 4.5^{+0.9}_{-0.4} \times 10^{44}\,\mathrm{erg\,s^{-1}}$ including the core). Uncertainties on the luminosities include those on the parameters of the best-fitting spectral models. The value of $L_{\rm X}$ given above for the *XMM–Newton* data with the central $0.15R_{500}$ excluded includes a correction for the redistribution of photons into and out of the excluded region by the *XMM–Newton* PSF. The same method used to calculated the redistribution factors for the temperature profile was used to calculate that the PSF redistribution leads to a net increase of 9 per cent in the number of photons detected in the $(0.15–1)R_{500}$ aperture. The measured luminosity was thus scaled down by this factor.

The global properties of XLSSC 029 are all consistent with those measured by Pacaud et al. (2007) using the original 20 ks of survey *XMM–Newton* data.

5 SCALING RELATION EVOLUTION

The hydrostatic mass estimate obtained for XLSSC 029 presents a unique opportunity to investigate the mass–observable scaling relations at $z > 1$. Recall that the gas mass and total mass were measured using a combination of the *XMM–Newton* and *Chandra* data, although the total mass estimate was strongly dependent on the *XMM–Newton* temperature profile. The global spectral properties were measured separately for *XMM–Newton* and *Chandra*, so data points for each satellite are included in the scaling relations that follow. In all cases, the data were scaled by an appropriate power of $E(z)$ [where $E^2(z) = \Omega_M(1+z)^3 + (1-\Omega_M-\Omega_\Lambda)(1+z)^2 + \Omega_\Lambda$, describing the redshift evolution of the Hubble parameter] to remove the predicted self-similar evolution in each relation. The exponent used for each relation is indicated in the figures below.

The mass and temperature of XLSSC 029 were compared with the data of Vikhlinin et al. (2006), derived from high-quality *Chandra* observations of low-redshift, relaxed clusters, and of Arnaud et al. (2005), derived from a similar *XMM–Newton* sample. The properties of XLSSC 029 were measured in a consistent manner to those of these local samples. The two data points for XLSSC 029 (for the *XMM–Newton* and *Chandra* temperatures) are plotted along with the local data in Fig. 8. Both XLSSC 029 data points are consistent with the local relations. Our data are also consistent with the mass–temperature relation measured by Kotov & Vikhlinin (2005) from *XMM–Newton* observations of clusters at $0.4 < z < 0.7$.

Next, the Y_X–M relation was investigated. Y_X, the product of the gas mass and temperature, has been shown to have a low-scatter scaling relation with cluster mass in simulated clusters (Kravtsov et al. 2006; Poole et al. 2007). Y_X was calculated for XLSSC 029, and was found to be $(6.1 \pm 1.3) \times 10^{13}\,M_\odot$ keV [using the *XMM–Newton kT*; the *Chandra kT* gave $(7.7 \pm 2.2) \times 10^{13}\,M_\odot$ keV]. These values are plotted on the local Y_X–M relations of Vikhlinin et al. (2006) and Arnaud, Pointecouteau & Pratt (2007) in Fig. 9. Again, the properties of XLSSC 029 are consistent with the local relation.

Finally, in Fig. 10 we plot XLSSC 029 on the L_X–M relation of Maughan (2007). This is a sample of 115 clusters over the redshift range $0.1 < z < 1.3$ observed with *Chandra*. For those clusters, the masses were estimated from their Y_X values. For XLSSC 029, however, we have the advantage that the mass was estimated from a full hydrostatic mass analysis. Once more, the properties of XLSSC 029 are consistent with the self-similar evolution of the cluster population.

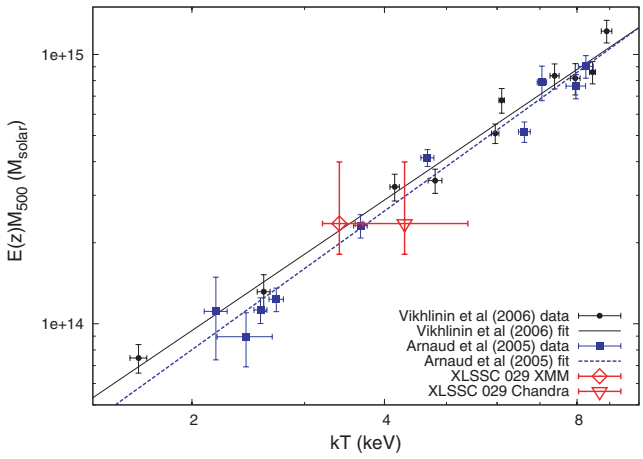

Figure 8. XLSSC 029 is plotted on the low-redshift mass–temperature relations of Arnaud et al. (2005) and Vikhlinin et al. (2006). The two XLSSC 029 points reflect the slightly different global temperatures measured with the *XMM–Newton* and *Chandra* data. The central 0.15 R_{500} was excluded from the temperature measurements.

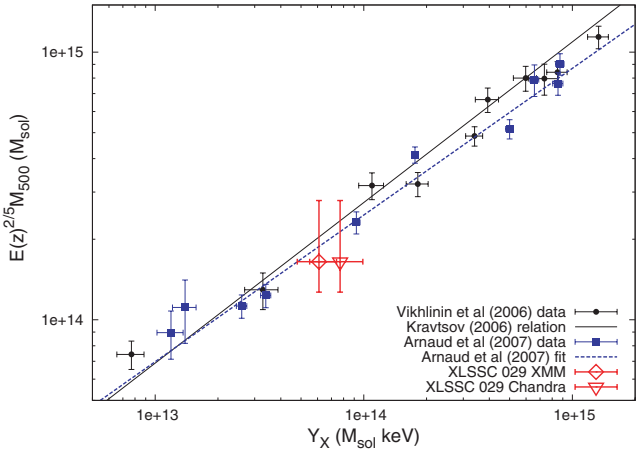

Figure 9. XLSSC 029 is plotted on the low-redshift Y_X–M relations of Arnaud et al. (2005) and Vikhlinin et al. (2006). The two XLSSC 029 points reflect the slightly different global temperatures measured with the *XMM–Newton* and *Chandra* data. The central $0.15R_{500}$ was excluded from the temperature measurements.

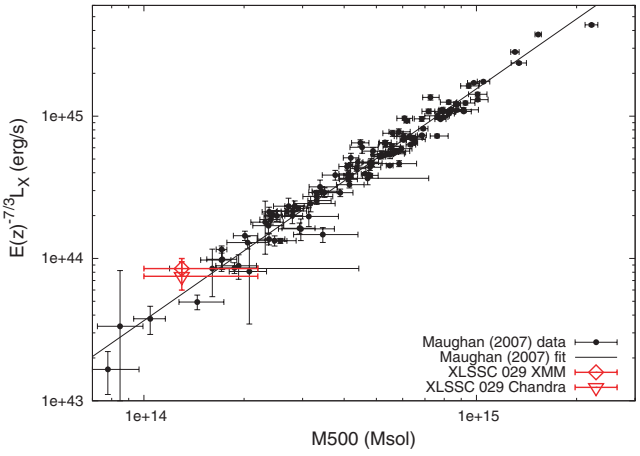

Figure 10. XLSSC 029 is plotted in the L_X–M relation of Maughan (2007). The two XLSSC 029 points reflect the slightly different luminosities measured with the *XMM–Newton* and *Chandra* data. The central $0.15R_{500}$ was excluded from the luminosity measurements.

6 DISCUSSION

The deep *XMM–Newton* and *Chandra* observations of XLSSC 029 have enabled a uniquely detailed study of a $z > 1$ galaxy cluster. This allows the comparison of the properties of XLSSC 029 with the expected evolution of the local cluster population. The iron abundance in XLSSC 029 is not tightly constrained by the data, but the value measured with the central $0.15R_{500}$ excluded is consistent with the observed and predicted evolution in ICM metal abundance (Ettori 2005; Balestra et al. 2007; Maughan et al. 2008). The increased metal abundance when the core regions are included, while not statistically significant, is also in line with the mean trends found by Maughan et al. (2008).

A key result from this analysis is the measurement of the temperature profile of XLSSC 029, providing the foundation for the hydrostatic mass analysis of the system. The accuracy of the *XMM–Newton* temperature profile is supported by the agreement of the cruder *Chandra* profile. The modelling of the temperature profile is a key step in the mass analysis, and we note that while the model used provides a good description of the radial temperature distribution in XLSSC 029, other models could also be used to fit the data. This is not a concern, as we do not require a physical interpretation of the individual model parameters; the model is simply used to give the value and gradient of the 3D temperature. Importantly we do not extrapolate our mass estimates beyond the range of the data, so the results are not strongly dependent on the choice of temperature profile model. That said, the model values from beyond the projected radial range of the data do have some effect on the fit, because gas from all external radii is projected along the line of sight in the fitting process. This effect is negligible because the low density of the gas at large radii minimizes its contribution to the projected temperature at the projected radii of interest.

As discussed in Section 3 the analysis of the X-ray images suggests that XLSSC 029 is a relatively relaxed cluster, particularly compared to the high-redshift cluster population. The X-ray mass estimate requires that the ICM is in hydrostatic equilibrium with the gravitational potential. While the X-ray morphology suggests that this is the case, there are examples of clusters with relaxed X-ray morphologies that show evidence for being out of hydrostatic equilibrium (e.g. CLJ1226.9+3332 at $z = 0.89$; Maughan et al. 2007). In the case of CLJ1226.9+3332, a temperature map showed asymmetric structure coincident with a subclump of galaxies detected in the optical images. The X-ray data are insufficient for a spectral map of XLSSC 029 (to achieve a similar quality map to that of CLJ1226.9+3332 would require almost 10 times the current *XMM–Newton* exposure), but the available optical data do not indicate substructure in the galaxy distribution.

Many relaxed clusters in the local Universe exhibit cool cores due to the short radiative cooling times in the central regions (e.g. Fabian 1994). The fraction of cool core clusters has been found to be significantly lower at redshifts higher than 0.5 (Vikhlinin et al. 2007). This is believed to be due to the higher incidence of cluster mergers at high redshift, with mergers disrupting the cooling process. The temperature profile of XLSSC 029 gives no indication of any cool core in the system. This could indicate that the system has recently undergone a merger event, or it could simply be because the gas in the cluster core has not had long enough to cool significantly. In order to investigate the latter possibility, the radiative cooling time of the ICM was calculated using the measured gas density and temperature profile according to

$$t_{\rm cool} = 8.5 \times 10^{10}\,{\rm yr} \left(\frac{n_{\rm p}}{10^{-3}\,{\rm cm}^{-3}}\right)^{-1} \left(\frac{T}{10^{8}\,{\rm K}}\right)^{1/2} \quad (3)$$

(Sarazin 1986), and the resulting profile is plotted in Fig. 11. The profile shows that the radiative cooling time of the ICM in XLSSC 029 is longer than the Hubble time (at $z = 1.05$) outside of the central ∼30 kpc, so even without recent merger activity, there may not have been sufficient time for a significant cool core to develop in this system.

The gas mass fractions measured for XLSSC 029 at R_{500} and R_{2500} are in good agreement with the corresponding values measured for the Vikhlinin et al. (2006) clusters. This is consistent with no evolution in $f_{\rm gas}$ in our assumed ΛCDM cosmology. With the reliable masses measured in these deep observations, XLSSC 029 can provide a useful high-redshift data point for cosmological studies that make use of $f_{\rm gas}$ evolution (Allen et al. 2004).

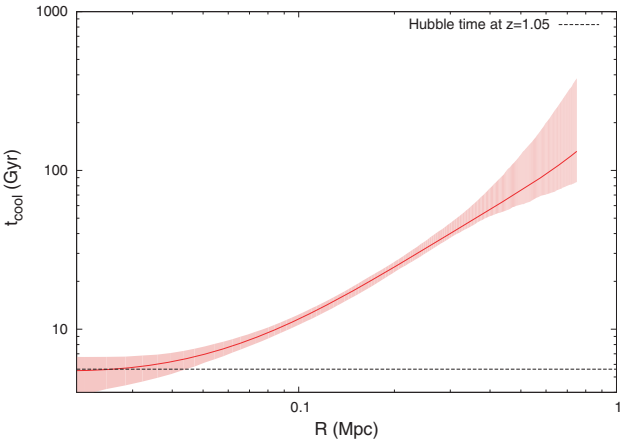

Figure 11. Cooling time profile of XLSSC 029. The shaded region shows the 1σ uncertainties, and the dashed line indicates the Hubble time at the redshift of XLSSC 029.

Perhaps the most interesting results from the study of XLSSC 029 are obtained by its use as a probe of the evolution of the mass–observable scaling relations. In all of the relations tested, the observable properties of XLSSC 029 were consistent with the self-similar evolution of the scaling relations. In particular, the agreement of XLSSC 029 with the $Y_{\rm X}$–M relation provides further support for the use of $Y_{\rm X}$ as a mass proxy for even the most distant clusters (see also Kravtsov et al. 2006; Maughan 2007). Furthermore, XLSSC 029 was found to lie on the $L_{\rm X}$–M relation of Maughan (2007). This provides additional support for their conclusion that $L_{\rm X}$ can be used as an effective mass proxy, as the mass of XLSSC 029 was estimated from a full hydrostatic analysis rather than from $Y_{\rm X}$ as in the Maughan (2007) sample.

A similar study was performed on the $z = 0.89$ cluster CLJ1226.9+3332, but that cluster was found to deviate from the self-similar scaling relations (Maughan et al. 2007). This was deemed likely to be due to merger activity in that cluster. In the case of XLSSC 029, the current data show no evidence for merger activity, but are not sufficiently deep to detect temperature substructure like that found in CLJ1226.9+3332. The relaxed appearance of XLSSC 029 and its agreement with the self-similar evolution of mass–observable relations form a self-consistent picture. However, it is possible that biases on our mass estimate due to a deviation from hydrostatic equilibrium and non-standard evolution could conspire to cancel one-another out.

7 CONCLUSIONS

Our hydrostatic X-ray mass analysis of XLSSC 029 has provided a unique opportunity to test the evolution of the mass–observable scaling relations at $z = 1$. While the strength of our conclusions is limited by the use of a single object, we found no evidence to reject the simple self-similar evolution of the scaling relations. This provides support for the use of these scaling relations in cosmological studies with large sample of distant clusters where the data do not allow such detailed mass analyses.

ACKNOWLEDGMENTS

We are grateful to the referee for several useful suggestions, particularly on improving the treatment of the *XMM–Newton* PSF.

BJM was supported during most of this work by NASA through *Chandra* Post-doctoral Fellowship Award Number PF4-50034 issued by the *Chandra* X-Ray Observatory Center, which is operated by the Smithsonian Astrophysical Observatory for and on behalf of NASA under contract NAS8-03060. SA acknowledges financial support from contract ASI-INAF I/023/05/0.

REFERENCES

Allen S. W., Schmidt R. W., Ebeling H., Fabian A. C., van Speybroeck L., 2004, MNRAS, 353, 457
Anders E., Grevesse N., 1989, Geochim. Cosmochim. Acta, 53, 197
Andreon S., Valtchanov I., Jones L. R., Altieri B., Bremer M., Willis J., Pierre M., Quintana H., 2005, MNRAS, 359, 1250
Arnaud M. et al., 2002, A&A, 390, 27
Arnaud M., Pointecouteau E., Pratt G. W., 2005, A&A, 441, 893
Arnaud M., Pointecouteau E., Pratt G. W., 2007, A&A, 474, L37
Balestra I., Tozzi P., Ettori S., Rosati P., Borgani S., Mainieri V., Norman C., Viola M., 2007, A&A, 462, 429
Birkinshaw M., 1999, Phys. Rep., 310, 97
Bremer M. N. et al., 2006, MNRAS, 371, 1427
Carter J. A., Read A. M., 2007, A&A, 464, 1155
Cavaliere A., Fusco-Femiano R., 1976, A&A, 49, L137
Cohen A. S. et al., 2003, ApJ, 591, 640
Dahle H., 2006, ApJ, 653, 954
Dickey J. M., Lockman F. J., 1990, ARA&A, 28, 215
Ebeling H., White D. A., Rangarajan F. V. N., 2006, MNRAS, 368, 65
Ettori S., 2005, MNRAS, 362, 110
Evrard A. E., Metzler C. A., Navarro J. F., 1996, ApJ, 469, 494
Fabian A. C., 1994, ARA&A, 32, 277
Finoguenov A., Reiprich T. H., Böhringer H., 2001, A&A, 368, 749
Henry J. P., 2004, ApJ, 609, 603
Kaiser N., 1986, MNRAS, 222, 323
Kotov O., Vikhlinin A., 2005, ApJ, 633, 781
Kotov O., Vikhlinin A., 2006, ApJ, 641, 752
Kravtsov A. V., Vikhlinin A., Nagai D., 2006, ApJ, 650, 128
Markevitch M., 1998, ApJ, 504, 27
Maughan B. J., 2007, ApJ, 668, 772
Maughan B. J., Jones C., Jones L. R., Van Speybroeck L., 2007, ApJ, 659, 1125
Maughan B. J., Jones C., Forman W., Van Speybroeck L., 2008, ApJS, 174, 117
Mullis C. R., Rosati P., Lamer G., Böhringer H., Schwope A., Schuecker P., Fassbender R., 2005, ApJ, 623, L85
Nagai D., Vikhlinin A., Kravtsov A. V., 2007, ApJ, 655, 98
O'Hara T. B., Mohr J. J., Bialek J. J., Evrard A. E., 2006, ApJ, 639, 64
Pacaud F. et al., 2007, MNRAS, 382, 1289
Pierre M. et al., 2004, J. Cosmol. Astro-Particle Phys., 9, 11
Pierre M. et al., 2006, MNRAS, 372, 591
Piffaretti R., Jetzer P., Schindler S., 2003, A&A, 398, 41
Poole G. B., Fardal M. A., Babul A., McCarthy I. G., Quinn T., Wadsley J., 2006, MNRAS, 373, 881
Poole G. B., Babul A., McCarthy I. G., Fardal M. A., Bildfell C. J., Quinn T., Mahdavi A., 2007, MNRAS, 380, 437
Reiprich T. H., Böhringer H., 2002, ApJ, 567, 716
Rosati P., Borgani S., Norman C., 2002, ARA&A, 40, 539
Rosati P. et al., 2004, ApJ, 127, 230
Sarazin C. L., 1986, Rev. Mod. Phys., 58, 1
Smith G. P., Kneib J.-P., Ebeling H., Czoske O., Smail I., 2001a, ApJ, 552, 493
Smith R. K., Brickhouse N. S., Liedahl D. A., Raymond J. C., 2001b, ApJ, 556, L91
Stanford S. A. et al., 2006, ApJ, 646, L13
Valtchanov I. et al., 2004, A&A, 423, 75
Vikhlinin A., 2006, ApJ, 640, 710
Vikhlinin A., McNamara B. R., Forman W., Jones C., Quintana H., Hornstrup A., 1998, ApJ, 502, 558
Vikhlinin A. et al., 2003, ApJ, 590, 15
Vikhlinin A., Markevitch M., Murray S. S., Jones C., Forman W., Van Speybroeck L., 2005, ApJ, 628, 655
Vikhlinin A., Kravtsov A., Forman W., Jones C., Markevitch M., Murray S. S., Van Speybroeck L., 2006, ApJ, 640, 691
Vikhlinin A., Burenin R., Forman W. R., Jones C., Hornstrup A., Murray S. S., Quintana H., 2007, in Böhringer H., Pratt G. W., Finoguenov A., Schuecker P., eds, ESO Astrophys. Symp., Heating Versus Cooling in Galaxies and Clusters of Galaxies. Springer-Verlag, Berlin, p. 48
Willis J. P. et al., 2005, MNRAS, 363, 675

This paper has been typeset from a TEX/LATEX file prepared by the author.